Spectroscopic signatures of tetralayer graphene polytypes

Andrew McEllistrim [*] and Aitor Garcia-Ruiz
National Graphene Institute, University of Manchester, Booth Street East, Manchester M13 9PL, United Kingdom and Department of Physics and Astronomy, University of Manchester, Oxford Road, Manchester M13 9PL, United Kingdom

Zachary A. H. Goodwin
National Graphene Institute, University of Manchester, Booth Street East, Manchester M13 9PL, United Kingdom; Department of Physics and Astronomy, University of Manchester, Oxford Road, Manchester M13 9PL, United Kingdom; and John A. Paulson School of Engineering and Applied Sciences, Havard University, Cambridge, Massachusetts 02138, USA

Vladimir I. Fal'ko
National Graphene Institute, University of Manchester, Booth Street East, Manchester M13 9PL, United Kingdom; Department of Physics and Astronomy, University of Manchester, Oxford Road, Manchester M13 9PL, United Kingdom; and Henry Royce Institute for Advanced Materials, University of Manchester, Oxford Road, Manchester M13 9PL, United Kingdom

(Received 16 February 2023; accepted 11 April 2023; published 26 April 2023)

Tetralayer graphene has recently become a new addition to the family of few-layer graphenes with versatile electronic properties. This material can be realized in three distinctive stacking configurations for which we determine spectroscopic signatures in angle-resolved photoemission spectroscopy, dynamical optical conductivity, and Raman spectra of interband excitations. The reported library of spectral features of tetralayer graphenes can be used for the noninvasive identification of the stacking order realized in a particular film.

DOI: 10.1103/PhysRevB.107.155147

I. INTRODUCTION

Although graphene has already been the subject of numerous experimental and theoretical studies, the family of few-layer graphene polytypes is still growing, showing various stacking-dependent electronic properties. In this respect, studies of bilayers and trilayers have received most of the attention, but, recently, the family of graphene polytypes got a new member: tetralayer graphene [1–11]. For tetralayer graphene (4LG), there are four possible interlayer stacking configurations with Bernal (AB or BA) stacking of adjacent layers. Two of those are related by inversion, leaving only three unique structures with their specific electronic band structures: ABAB (Bernal 4LG), ABCA (rhombohedral 4LG), and an allusive ABCB or ABAC (mixed-stacking 4LG) [2]. The latter mixed-stacking 4LG is an interesting system as it appears to be the thinnest few-layer graphene that has neither inversion nor mirror plane ($z \to -z$) symmetry, which allows it to possess a spontaneous out-of-plane electric polarization. To mention, these four structures can be obtained from each other by shear displacements of the layers [12], and they also appear in pairs across moiré patterns in flakes of small-angle-twisted tetralayers, produced by mechanically transferring a monolayer on a trilayer [13] or by assembling together two aligned bilayer flakes [12,14]. All of this leads to the necessity to develop a set of nonnvasive characterisation methods to identify local stacking orders in tetralayer graphenes.

In this paper, we analyze spectroscopic responses of tetralayer graphene systems from angle-resolved photoelectric spectroscopy (ARPES), optical visibility in the infrared range and electronic Raman scattering. The below-reported results are obtained using a hybrid $\boldsymbol{k}\cdot\boldsymbol{p}$ theory-tight-binding approach, described in Sec. II, based on a fully-parametrized Slonczewski-Weiss-McClure model of graphite [15–18] with each of the spectroscopic characteristics discussed separately in Secs. III–V, respectively.

II. BAND STRUCTURE OF TETRALAYER GRAPHENES

Tetralayer graphene can exist in four types of stacking orders, depending on the relative shifts between adjacent layers. In the Bernal configuration, the carbons atoms in layers 1 and 3 occupy identical positions, whereas they are laterally shifted by $\boldsymbol{\tau} = (0, a/\sqrt{3})$ with respect to layers 2 and 4, $a \approx 2.46$ Å being the lattice constant of graphene. In the rhombohedral configuration, each layer is shifted by $\boldsymbol{\tau}$ with respect to the top adjacent layer. Tetralayer graphite allows for another type of configuration that features sequences of Bernal and rhombohedral arrangement. In this mixed configuration, also known as ABCB (ABAC), the graphene layer 4 (3) lies directly on top of layer 2 (1), whereas the first and third (second and fourth) are shifted by $\boldsymbol{\tau}$ and $-\boldsymbol{\tau}$, respectively.

Electronic properties for each of these configurations can be determined using the hybrid $\boldsymbol{k}\cdot\boldsymbol{p}$ theory-tight-binding

[*] andrew.mcellistrim@postgrad.manchester.ac.uk

Hamiltonians [15–17],

$$\mathcal{H}_{\mathrm{ABAB}} = \begin{pmatrix} H_g + \frac{\Delta'}{2}(\mathbb{1}_2 + \sigma_z) & V_{\mathrm{AB}} & W_{\mathrm{ABA}} & 0 \\ V_{\mathrm{AB}}^\dagger & H_g + \Delta'(\mathbb{1}_2 - \sigma_z) & V_{\mathrm{AB}}^\dagger & W_{\mathrm{BAB}} \\ W_{\mathrm{ABA}}^\dagger & V_{\mathrm{AB}} & H_g + \Delta'(\mathbb{1}_2 + \sigma_z) & V \\ 0 & W_{\mathrm{BAB}}^\dagger & V_{\mathrm{AB}}^\dagger & H_g + \frac{\Delta'}{2}(\mathbb{1}_2 - \sigma_z) \end{pmatrix}, \tag{1a}$$

$$\mathcal{H}_{\mathrm{ABCA}} = \begin{pmatrix} H_g + \frac{\Delta'}{2}(\mathbb{1}_2 + \sigma_z) & V_{\mathrm{AB}} & W_{\mathrm{ABC}} & 0 \\ V_{\mathrm{AB}}^\dagger & H_g + \Delta'\mathbb{1}_2 & V_{\mathrm{AB}} & W_{\mathrm{ABC}} \\ W_{\mathrm{ABC}}^\dagger & V_{\mathrm{AB}}^\dagger & H_g + \Delta'\mathbb{1}_2 & V \\ 0 & W_{\mathrm{ABC}}^\dagger & V_{\mathrm{AB}}^\dagger & H_g + \frac{\Delta'}{2}(\mathbb{1}_2 - \sigma_z) \end{pmatrix}, \tag{1b}$$

$$\mathcal{H}_{\mathrm{ABCB}} = \begin{pmatrix} H_g + \frac{\Delta'}{2}(\mathbb{1}_2 + \sigma_z) & V_{\mathrm{AB}} & W_{\mathrm{ABC}} & 0 \\ V_{\mathrm{AB}}^\dagger & H_g + \Delta'\mathbb{1}_2 & V_{\mathrm{AB}} & W_{\mathrm{ABA}} \\ W_{\mathrm{ABC}}^\dagger & V_{\mathrm{AB}}^\dagger & H_g + \Delta'(\mathbb{1}_2 + \sigma_z) & V_{\mathrm{AB}}^\dagger \\ 0 & W_{\mathrm{ABA}}^\dagger & V_{\mathrm{AB}} & H_g + \frac{\Delta'}{2}(\mathbb{1}_2 + \sigma_z) \end{pmatrix}, \tag{1c}$$

$$\mathcal{H}_{\mathrm{ABAC}} = \begin{pmatrix} H_g + \frac{\Delta'}{2}(\mathbb{1}_2 + \sigma_z) & V_{\mathrm{AB}} & W_{\mathrm{ABA}} & 0 \\ V_{\mathrm{AB}}^\dagger & H_g + \Delta'(\mathbb{1}_2 - \sigma_z) & V_{\mathrm{AB}} & W_{\mathrm{ABC}}^\dagger \\ W_{\mathrm{ABA}}^\dagger & V_{\mathrm{AB}}^\dagger & H_g + \Delta'\mathbb{1}_2 & V_{\mathrm{AB}}^\dagger \\ 0 & W_{\mathrm{ABC}} & V_{\mathrm{AB}} & H_g + \frac{\Delta'}{2}(\mathbb{1}_2 + \sigma_z) \end{pmatrix}, \tag{1d}$$

$$H_g = \begin{pmatrix} 0 & v\pi_\xi^* \\ v\pi_\xi & 0 \end{pmatrix}, \quad V_{\mathrm{AB}} = \begin{pmatrix} -v_4\pi_\xi & \gamma_1 \\ -v_3\pi_\xi^* & -v_4\pi_\xi \end{pmatrix}, \quad \pi_\xi \approx \xi p_x + i p_y$$
$$W_{\mathrm{ABA}} = \begin{pmatrix} \frac{\gamma_5}{2} & 0 \\ 0 & \frac{\gamma_2}{2} \end{pmatrix}, \quad W_{\mathrm{BAB}} = \begin{pmatrix} \frac{\gamma_2}{2} & 0 \\ 0 & \frac{\gamma_5}{2} \end{pmatrix}, \quad W_{\mathrm{ABC}} = \begin{pmatrix} 0 & 0 \\ \frac{\gamma_2}{2} & 0 \end{pmatrix}, \quad \sigma_z = \begin{pmatrix} 1 & 0 \\ 0 & -1 \end{pmatrix}. \tag{1e}$$

Here $\mathbb{1}_2$ is the 2×2 identity matrix, and $\boldsymbol{p} = (p_x, p_y)$ is the momentum measured from the corners of the Brillouin zone, $K_\xi = \frac{4\pi}{3a}(\xi, 0)$. In the above equations, we use the following values [19,20] for the coupling parameters: $(v, v_3, v_4) = (1, 0.1, 0.022)10^6$ m/s and $(\gamma_1, \gamma_2, \gamma_5, \Delta') = (390, -17, 38, 25)$ meV.

The band structure of all of these systems can be calculated by diagonalizing the above Hamiltonians. Within the three polytypes of 4LG, each band structure has defining characteristics that can be related to the density of states (DoS). Bernal 4LG is unique as it has the lowest-energy appearance of its $3^\pm$ band edges at $\boldsymbol{p}$=**0**, seen as a step at $\gamma_1/\varphi + \sqrt{2}\Delta'$ meV in the DoS, where φ is the golden number. It also has a comparatively large gap between this and its $4^\pm$ band edge. Rhombohedral is the only polytype without a Bernal stack in its configuration, thus, the only structure with just bands $1^\pm$ in its low-energy dispersion (see large van Hove singularity (vHs) at 0 meV). Additionally, rhombohedral contains a Mexican hatlike dispersion at an energy of $\pm\gamma_1 + \Delta'$ where the minimum of the band edge is off the $\boldsymbol{p}$=**0** line. The mixed stacking order has features of both Bernal and rhombohedral graphenes. First, it has two pairs of degenerate bands in its low-energy dispersion ($1^\pm$, $2^\pm$), such as Bernal and it has its $3^\pm$ band edge emerging at $\pm\gamma_1 + \Delta'$, such as in rhombohedral graphene [21]. This commonality in the $1^\pm, 2^\pm$ bands with Bernal is mirrored by a small vHs at 0 meV in the DoS. The position of the $3^\pm$ band can be seen as a step in the DoS plots coinciding with the vHs of rhombohedral at the same energy.

III. ARPES SPECTRA OF 4LGS

In ARPES experiments, a sample is irradiated by a source of high-energy photons ($\omega \approx 60$–100 eV), which eject electrons due to the photoelectric effect [22]. Because it is possible to trace back the energy and momentum of the scattered electrons, this technique allows us to reconstruct the dispersion of materials, and due to its surface sensitivity, it has been widely employed to study two-dimensional (2D) physics, such as transition-metal-dichalcogenides [23], surface states in topological insulators [24,25], and graphene systems [26].

Following previous works [27], we compute ARPES as

$$\mathcal{A}^n(E, \boldsymbol{p}) = \left| \sum_{\lambda=0}^{3} \sum_s F^\lambda \int d\boldsymbol{r}\, e^{-\frac{i}{\hbar}(\hbar \boldsymbol{K}_\xi^{(0)} + \boldsymbol{p}_\mathrm{w})\cdot \boldsymbol{r}} \psi_{\lambda_s}^n(\boldsymbol{p}) \right|^2 \times \frac{f(E - \epsilon_{\boldsymbol{p}}^n)\Gamma/\pi}{(\epsilon_{\boldsymbol{p}}^n - E)^2 + \Gamma^2}. \tag{2}$$

Here, $\psi_{\lambda_s}^n(\boldsymbol{p})$ is multicomponent wave function composed of the electron wave amplitudes on $s = A/B$ sublattices in each layer λ of a Bloch state at the point $\hbar\boldsymbol{K}_\xi^{(0)} + \boldsymbol{p}_\mathrm{w}$ in the Brillouin zone of graphene. Indices nth identify valence (n^-) and conduction (n^+) bands in the few-layer graphene spectrum, and $f(E - \epsilon_{\boldsymbol{p}}^n)$ is the Fermi distribution. We also introduce a factor $F = |F| e^{\frac{i}{\hbar} p_z c_0}$ in Eq. (2) above, where $|F| = 0.4$ accounts for the attenuating effect of ejecting electrons from layers further away from the top layer ($\lambda = 0$), and the phase factor accounts for the mutual phase shifts acquired by the partial waves of electrons originating (with an out-of-plane momentum p_z) in different layers ($\lambda > 0$) (we use $c_0 = 3.35$ Å as the interlayer distance in graphitic films). Equation (2) states that the observable ARPES intensity is determined by the interference of electron waves originating

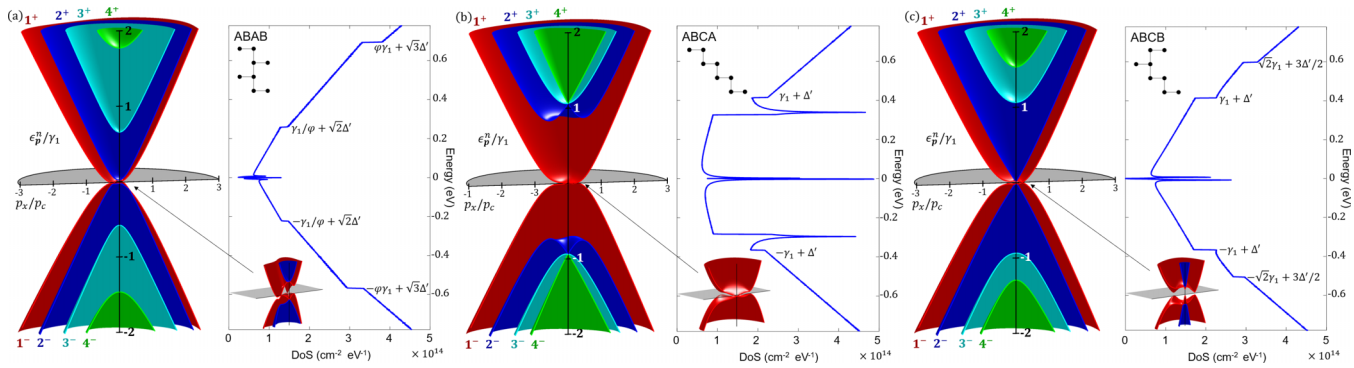

FIG. 1. Band structure and density of states (DoS) of (a) Bernal, (b) rhombohedral, and (c) mixed tetralayer graphene. The insets at the bottom left of the DoS show the low-energy band structure within an energy window of ±30 meV. The effect of Δ' becomes apparent at the edges of the bands $3^{\pm}$ and $4^{\pm}$ at $\boldsymbol{p} = \mathbf{0}$, which induces steps in the DoS. In the labels of panel (a) $p_c = \gamma_1/v$ and $\varphi \equiv \frac{1+\sqrt{5}}{2}$.

from the A and B sublattices of each of the four layers, and it takes into account inelastic broadening and spectrometer resolution, $\Gamma = 60$ meV.

In Fig. 2(a), we show three sets of ARPES maps for Bernal, rhombohedral, and mixed-stacking 4LGs. The set of four images on the top show momentum cuts through the K point in the k_y direction. These images directly coincide with the band structures presented in Fig. 1. All other images are the constant energy maps on the $p_x - p_y$ (around the K point), which reflect the layer and sublattice compositions of the electronic wave functions. Their appearance in ARPES depends on the energy ω of the incoming photon as that determines the out-of-plane momentum of the excited electrons $p_z = \sqrt{2m(\omega - A) + \epsilon_c - (\hbar K)^2}$, where ϵ_c is the energy the ARPES measurement was taken at. We estimate that $\omega \approx 70$ eV corresponds to a 4π phase shift for electron waves originating from two consecutive monolayers and $\omega \approx 100$ eV to a 5π phase shift (see Appendix B for a detailed calculation of the phase shift). The corresponding ARPES patterns for these two choices of photon energies are shown in rows 2–5 of Fig. 2 for constant energy maps at 250 and 500 meV below the Fermi level in the material.

We suggest that one can use the above spectra to identify each polytype by its unique signatures. We can identify Bernal graphene by the appearance of its third band as stated in Sec. II. We can see this in the constant momentum cut and −250 meV constant energy cut. To identify the rhombohedral poly type we see that only one band is present at 0 meV in the constant momentum cut. Finally, we can distinguish the mixed stacking orders by the intensity of their third and fourth valence bands in the constant energy cuts in the former the fourth band is clearly visible, particularly, at a photon energy of 100 eV. In ABCB, the third valence band has a far higher intensity than ABAC, particularly, at 100 eV photon energy. Note that, whereas both forms of mixed-stacking configuration, ABCB and ABAC, give an identical band structure, their ARPES spectral features are different [see Fig. 2(a)]. This is because the the ARPES signal coming from layers away from the surface is attenuated and captured in Eq. (2) by the factor F^{λ}. This breaks the symmetry in the z direction and making ARPES the only spectroscopy analyzed in this paper that enables us to distinguish the stacking orientation of this polytype of the tetralayer.

Finally, as in the experimentally fabricated material, the number of layers may vary across the flake, we also show (for comparison) the calculated ARPES maps for trilayer graphenes (ABA and ABC) in Fig. 2(b). We do not compare the 4LG spectra with the spectra of thicker crystals (pentalayers) as their appearance in ARPES is strongly affected by attenuation of electron waves emitted by deeper layers.

IV. OPTICAL CONDUCTIVITY

Optical conductivity characterizes response of a 2D film to light [28–31]. In particular, its real part describes absorption processes where energy ω of an incoming photon is spent in the formation of an electron-hole pair [32], whereas the imaginary part gives us insights into the phase shift of the scattered light [33]. Because these processes are very sensitive to the band structure as well as the energy and polarization of the incoming light, optical absorption is widely used to investigate different aspects of graphene systems [34], such as identifying the number of layers in graphene stacks [35] or determining the Slonczewski-Weiss-McClure parameters [21].

In this section, we compute the optical conductivity of graphene stacks with N layers due to interband excitations. Denoting $\boldsymbol{l} = (l_x, l_y)$ and l_z as the components of the polarization of light parallel and perpendicular to the sample, the optical conductivity takes the form [36–39]

$$O_{\parallel}(\omega) = \frac{i4}{\omega}\int \frac{d\boldsymbol{p}}{(2\pi\hbar)^2}\sum_{n_i,n_f}\frac{f\left(\epsilon_{\boldsymbol{p}}^{n_i^-}\right) - f\left(\epsilon_{\boldsymbol{p}}^{n_f^+}\right)}{\omega - \left(\epsilon_{\boldsymbol{p}}^{n_f^+} - \epsilon_{\boldsymbol{p}}^{n_i^-}\right) + i\eta^+}\left|\left\langle\psi_{\boldsymbol{p}}^{n_f^+}\right| e\boldsymbol{l}\cdot\frac{\partial\mathcal{H}}{\partial\boldsymbol{p}}\left|\psi_{\boldsymbol{p}}^{n_i^-}\right\rangle\right|^2, \tag{3a}$$

$$O_{\perp}(\omega) = i4\omega\int \frac{d\boldsymbol{p}}{(2\pi\hbar)^2}\sum_{n_i,n_f}\frac{f\left(\epsilon_{\boldsymbol{p}}^{n_i^-}\right) - f\left(\epsilon_{\boldsymbol{p}}^{n_f^+}\right)}{\omega - \left(\epsilon_{\boldsymbol{p}}^{n_f^+} - \epsilon_{\boldsymbol{p}}^{n_i^-}\right) + i\eta^+}\left|\left\langle\psi_{\boldsymbol{p}}^{n_f^+}\right| \sigma_0\otimes\tau\left|\psi_{\boldsymbol{p}}^{n_i^-}\right\rangle\right|^2, \tag{3b}$$

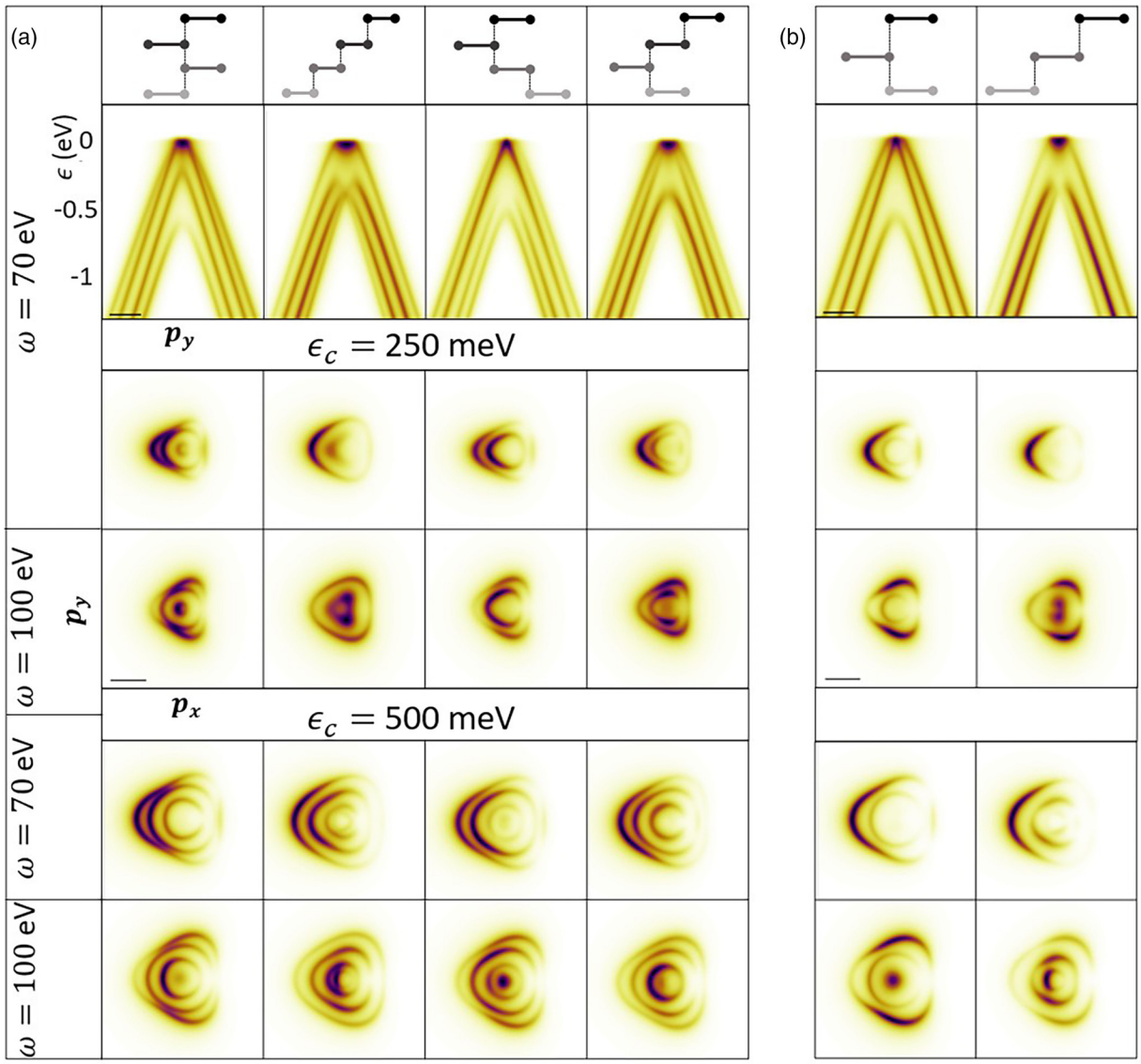

FIG. 2. (a) 4LG spectra, (b) 3LG sprectra. Row 1: Constant momentum cuts through the K_+ point, ω=70 eV. Row 2(3), constant energy maps at $\epsilon_c = -250$ meV and ω=70(100) eV. Row 4(5), constant energy maps at ϵ_c=500 meV and ω=70(100) eV. In all plots, the scale bar is 0.1 Å.

respectively. Above, η^+ is a positive infinitesimal, σ_0 is the unit matrix in the sublattice space, $\tau \equiv \mathrm{diag}(1, 2, \ldots, N)ed$, acting on the layer space is the dipole moment operator, and n_i^- (n_f^+) is the band index of the initial (final) states involved in the electronic transition, respectively.

In Fig. 3(a), we present the real and imaginary parts of the in-plane optical conductivity of the three different stacking configurations of tetralayer graphene in units of the optical absorption of graphene $O_\parallel^0 = \frac{1}{4\pi\varepsilon_0}\frac{\pi e^2}{\hbar c}$. In all configurations, transitions $n^- \to n^+$ are strongly suppressed, and for photon energies $\omega \sim 1$ eV, the absorption spectra are identical and equal to the nominal value of four decoupled graphene layers. In turn, for $\omega < 2\gamma_1$, the three absorption spectra exhibit strong differences, which stem from the distinctive features of their corresponding band structure (see Fig. 1). In particular, Bernal and ABCB tetralayer graphenes feature four peaks, produced by transitions between the bands close to the Fermi level and the high-energy bands. As mentioned Sec. II, the edges of the split bands in both the valence and the conduction side, are linearly shifted by the parameter Δ'. This results in transitions $1^- \to 3^+, 4^+$ being systematically more energetic than $3^-, 4^- \to 1^+$, and provides an experimental route for the determination of Δ'. Conversely, the spectrum of its rhombohedral counterpart is characterized by a sharp peak produced by transitions between the flat bands and the van Hove singularity in the Mexican-hat bands.

In Fig. 3(b), we present the real part of the optical response to perpendicularly polarized light. As opposed to in-plane polarized light, in this case, the main contribution comes from transitions $n^- \to n^+$, thus, providing complementary information about energy distances between edges of mirrored bands in the valence and the conduction sides. For photon energies ~1 eV, all spectra resemble that of three independent graphene bilayers $3O_\perp^0$ [38], whereas it is again at midinfrared

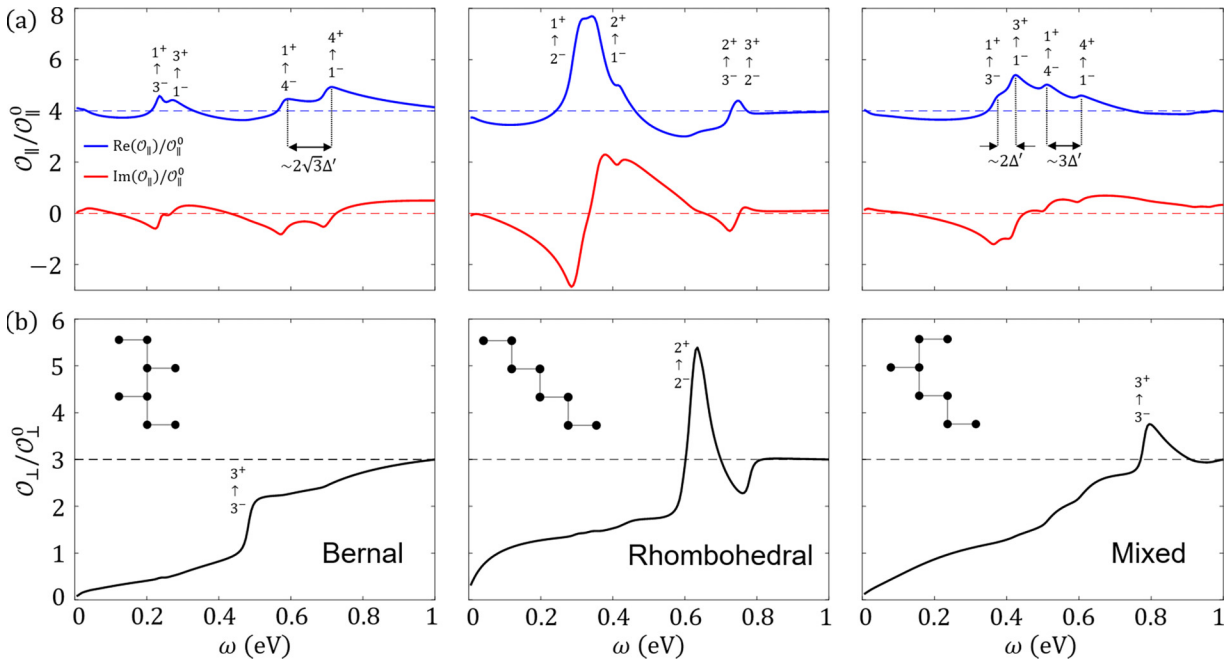

FIG. 3. (a) Real and imaginary parts of the in-plane optical conductivity of tetralayer graphenes in units of the universal optical absorption of graphene, $O_\parallel^0 = \frac{1}{4\pi\varepsilon_0}\frac{\pi e^2}{\hbar c}$. Transitions from $1^- \to 3^+, 4^+$ give rise to a peak that lies at higher energies than those from $3^-, 4^- \to 1^+$, due to the electron-hole asymmetry and the shift produced by Δ' in the band structure. (b) Real part of the out-of-plane optical response of tetralayer graphenes in units of the high-energy out-of-plane response of bilayer graphene, $O_\perp^0 = \frac{c_0^2\gamma_1^2}{2\hbar^2 v^2} O_\parallel^0$ [38] with an asymptotic value of $3O_\perp^0$ in all cases. The dominant contribution comes from transitions $n^- \to n^+$.

frequencies where the absorption spectra give us information about distinct features of the dispersion. In particular, the steplike feature at 0.5 eV of the Bernal absorption spectrum corresponds to the energy difference between states at the edges of the third bands, and the peaks at ∼0.6 and 0.8 eV in the rhombohedral and ABCB counterparts are linked to transitions that connect the Mexican-hat-shaped bands and heavy-mass bands in the valence and the conduction sides as shown in Figs. 1(b) and 1(c), respectively.

Finally, owing to the experimental challenge of fabricating films with a given thickness [34], we also present the results for three- and five-layer films in Figs. 4(a) and 4(b), respectively, for all possible stacking arrangements. For three-layer films, the in-plane absorption spectra of both rhombohedral and Bernal feature a peak at 0.4 and 0.6 eV, split by $\sim 2\Delta'$ and $\sim 3\Delta'$, respectively. In turn, the most distinctive feature for the out-of-plane absorption spectra is found in the ABC film, a strong peak at $2\gamma_1$. For five layers, as shown in the middle panels of Fig. 4(b), there are six possible stacking orders as both rhombohedral (top) or Bernal (bottom) may appear with a stacking fault in the outermost layer (second and fifth panels) or in the middle layer (middle two panels). We note that films with the largest stacking sequences of rhombohedral order feature sharper peaks, and they also lie at lower energies both in the in-plane and the out-of-plane absorption spectrum. This is because the flatness of bands closer to the Fermi level increases with the number of rhombohedral-stacked layers, and the bottoms of the sombrerolike bands also appear at lower energies. This contrasts with the spectra of films with larger stacks in the Bernal configuration, which tend to give a featureless constant absorption amplitude.

V. ELECTRONIC RAMAN SCATTERING

Raman spectroscopy, based on inelastic scattering of photons, also allows us to get the excitation fingerprint of two-dimensional materials [40]. In graphene materials, the strongest Raman signals originate from lattice excitations [41], i.e., phonons, and they provide a wealth of information about the nature of defects [42], the number of layers [43], or the presence of strain in the sample [44]. However, during the past decade, experiments have shown evidence for another type of excitation: the creation of electron-hole pairs [45]. Although this type of electronic Raman scattering (ERS) produces weaker signals, they come exclusively from the excitation spectra of electrons, and, therefore, they provide direct information about the band structure of graphene systems, such as the position of van Hove singularities [46,47] or the formation of gaps [48].

In this section, we model the ERS signals of the three polytypes of tetralayer graphene films presented in Sec. II. In particular, we study the ERS amplitude coming from two-step processes, which were shown to be the dominant contribution in graphene systems [45]. This amplitude is given by the evaluation of the two Feynman diagrams in the inset of Fig. 5, which involve: (i) the absorption (emission) at time t of a photon with energy ω ($\tilde{\omega}$) by an electron from an occupied state in the band with energy $\epsilon_{\boldsymbol{p}}^{n_i^-}$, which is excited into a virtual state and (ii) emission (absorption) at time t' of a photon with energy $\tilde{\omega}$ (ω) and one electronic transition into the final state with energy $\epsilon_{\boldsymbol{p}}^{n_f^+}$. The amplitude of such a process that results in an electron-hole pair with energy $\Delta\omega \equiv \omega - \tilde{\omega} = \epsilon_{\boldsymbol{p}}^{n_f^+} - \epsilon_{\boldsymbol{p}}^{n_i^-}$ is proportional

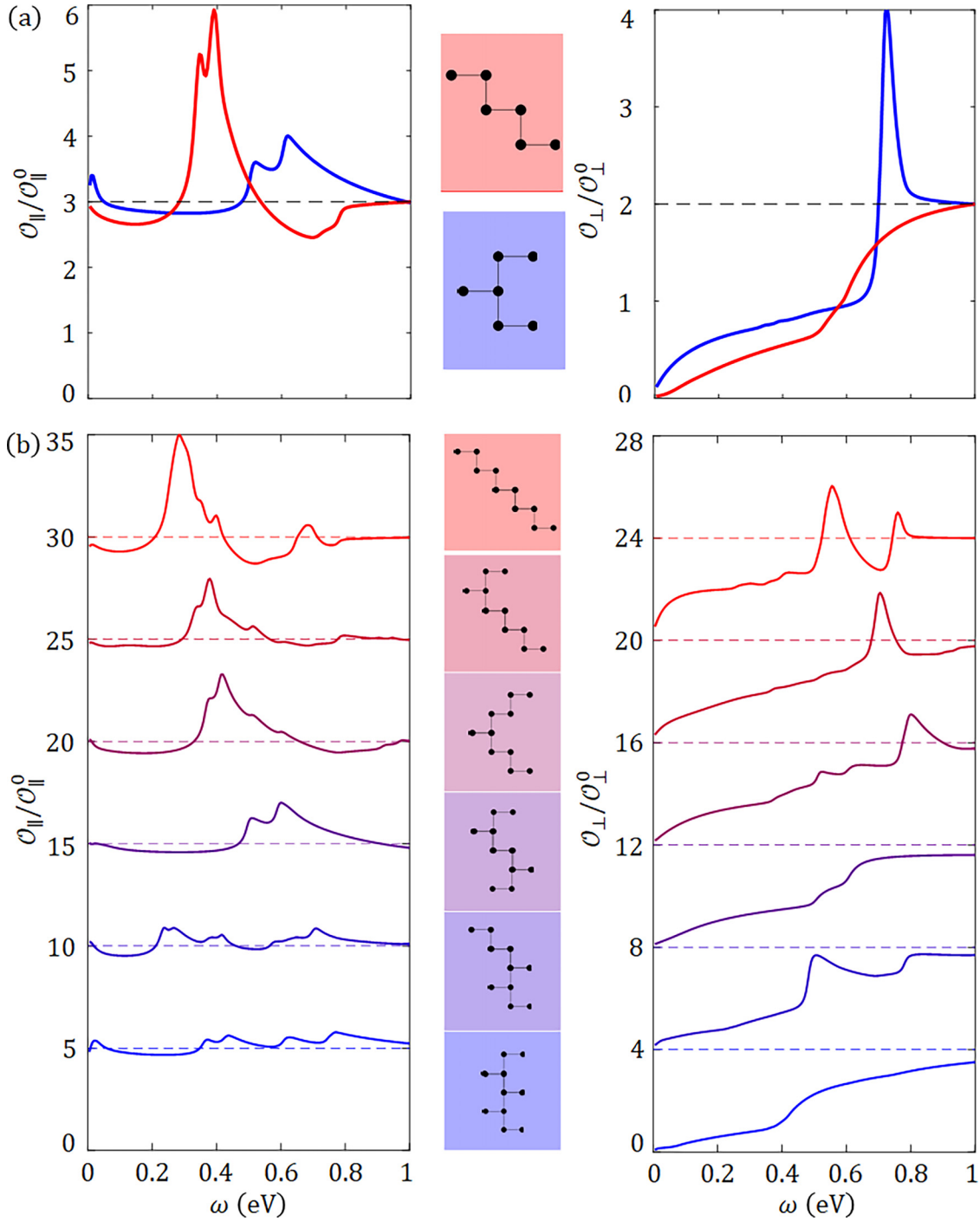

FIG. 4. Real part of the in-plane (left) and out-of-plane (right) optical conductivity for all possible configurations of (a) trilayer graphene and (b) pentalayer graphene. For clarity, plots for the parallel and perpendicular optical conductivities of pentalayer graphene are shifted by $5O_\parallel^0$ and $4O_\perp^0$, respectively.

to

$$\mathcal{R}(\Delta\omega) \propto |(\boldsymbol{l} \times \tilde{\boldsymbol{l}}^*)_z|^2 \sum_{n_f,n_i} \int \frac{d\boldsymbol{p}}{(2\pi\hbar)^2} [f(\epsilon_{\boldsymbol{p}}^{n_i^-}) - f(\epsilon_{\boldsymbol{p}}^{n_f^+})] \times \left| \langle \psi_{\boldsymbol{p}}^{n_f^+} | \mathbb{1}_4 \otimes \sigma_z | \psi_{\boldsymbol{p}}^{n_i^-} \rangle \right|^2 \delta(\epsilon_{\boldsymbol{p}}^{n_f^+} - \epsilon_{\boldsymbol{p}}^{n_i^-} - \Delta\omega), \tag{4}$$

where $\mathbb{1}_4$ is the 4×4 identity matrix acting on the layer space and σ_z is the third Pauli matrix acting on the sublattice space. To mention, the prefactor in the equation above determines the selection rules for the polarization of the scattered light, which needs to be perpendicular to that of the incoming light. This is the hallmark of ERS in graphene materials [45,49].

The ERS spectra for the three configurations of tetralayer graphene are shown in Fig. 5. It originated from electronic transitions that connect the n valence band with the

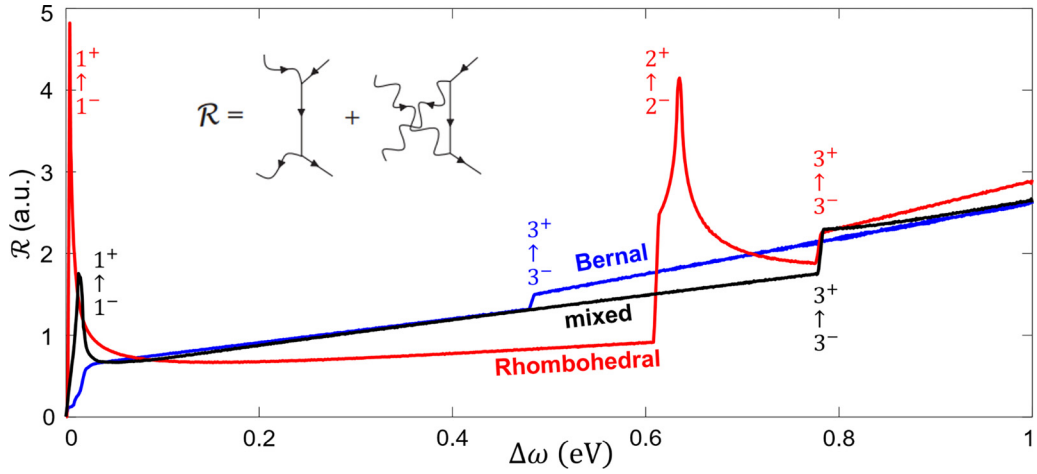

FIG. 5. Electronic contribution to Raman scattering in Bernal (blue), rhombohedral (red) and mixed-stacking (black) tetralayer graphene. The inset shows the diagrammatic representation of two-step processes.

n conduction band [49] as opposed to optical absorption where these transitions are forbidden, a common feature of graphene-based systems [50]. Accordingly, because electron-hole asymmetry is weak, ERS spectra have approximately the same functional form as the DoS, with the same spectral features, such as peaks and steps but at twice the energy. For example, in Bernal tetralayer graphene, we observe a linear trend with a small step at $2\gamma_1/\varphi \approx 500$ meV, which corresponds to the energy gap between the parabolic edges of the second conduction and valence bands in Fig. 1(a). In contrast, the ERS spectrum of rhombohedral tetralayer graphene features a sharp peak near the origin, due to transitions between flat bands, and at ∼650 meV, which is the distance between the edges of the Mexican-hat bands in Fig. 1(b). Finally, we see in the black curve of Fig. 5 that the low-energy electronic excitation spectrum of tetralayer films in mixed configuration generate a peak at ∼15 meV, followed by a linear trend and a step at $\sim 2\gamma_1$ from which the spectra of the three tetralayer films become indistinguishable.

For completeness, we also present the ERS spectra of graphene films composed of three or five layers in Fig. 6. For the former, we see that in the $3L$ rhombohedral spectra the $3^- \to 3^+$ step is no longer present and a shift of the $2^- \to 2^+$ to higher energy. In contrast, the parabolic split bands in Bernal trilayer graphene, which produce steps in the DoS at $\sim 3\Delta'/2 \pm \sqrt{2}\gamma_1$ (see Fig. 7), should also generate a step at $2\sqrt{2}\gamma_1 \approx 1.1$ eV in the ERS spectrum, which lies outside the energy range shown in our figures. For the latter, we observe that films with larger stacks in rhombohedral sequences feature peaks generated by electronic transitions from and to the Mexican-hat bands, whereas parabolic band edges, a common characteristic of films featuring Bernal-stacked layers, result in steps in the ERS intensity.

VI. CONCLUSION

Here we have studied the spectroscopic signatures of the three stacking polytypes of tetralayer graphene. We identify the unique features of each polytype for the different spectroscopic methods investigated. These calculations offer a reference library for the identification of tetralayer graphene polytypes, which offer rich physics—partly due to wide flat intervals in their low-energy bands

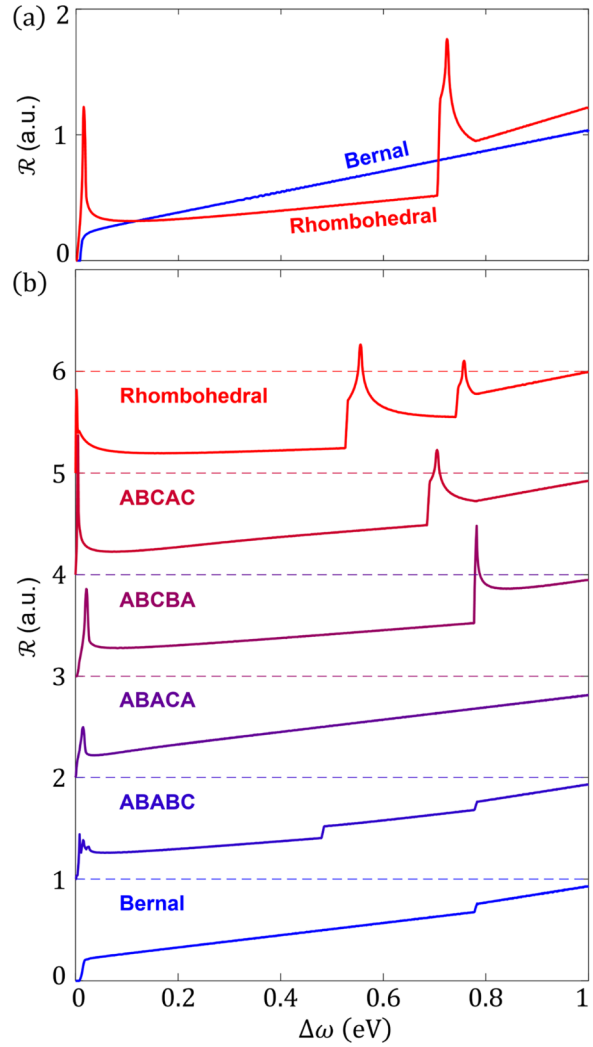

FIG. 6. (a) ERS signal for Bernal (blue) and rhombohedral 3LG. (b) ERS signal for the six distinct polytypes of 5LG. Each plot is shifted by one unit for clarity.

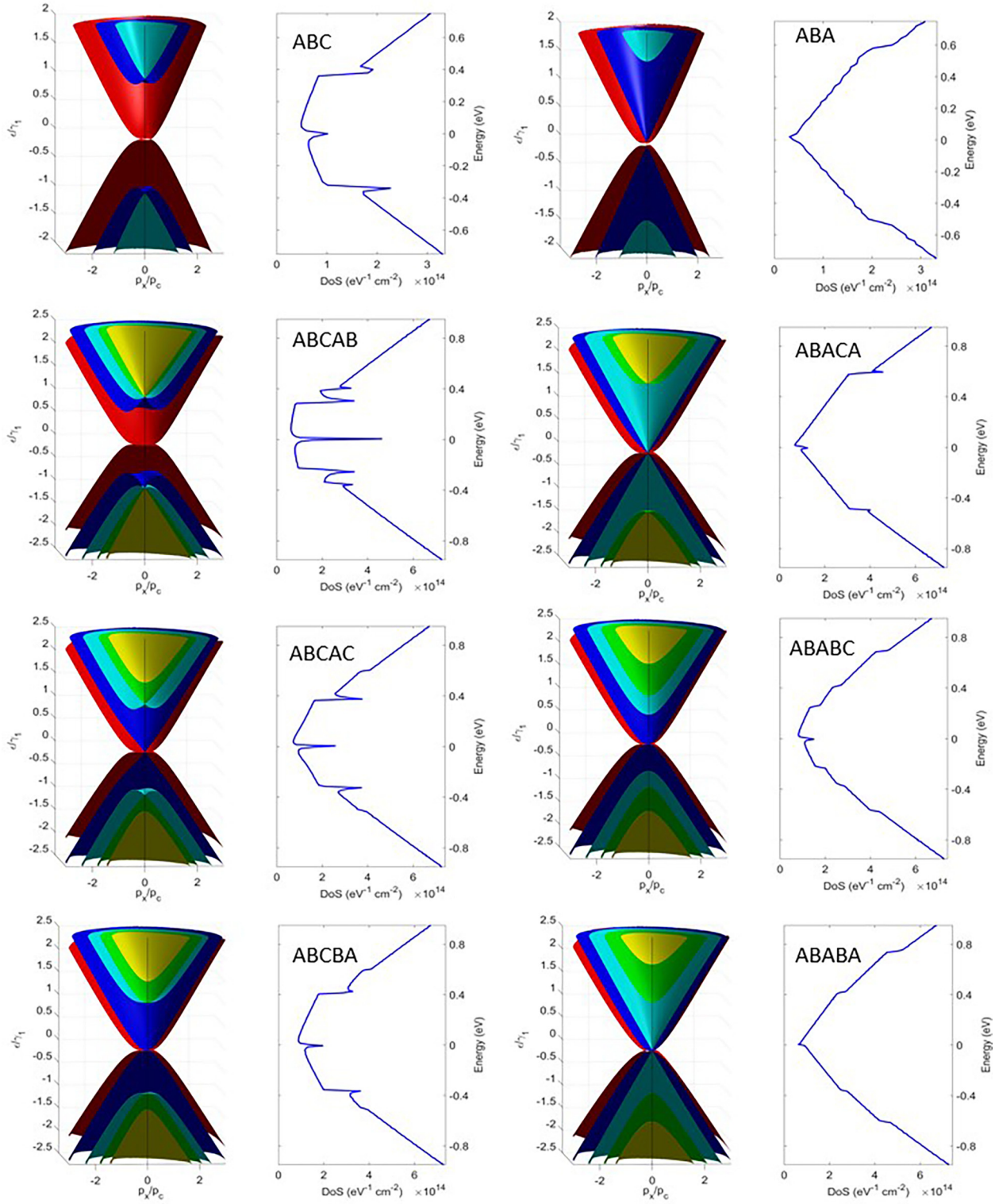

FIG. 7. Band structure and density of states of all trilayer and pentalayer graphene polytypes. In the labels of each panel $p_c = \gamma_1/v$.

and partly due to the broken symmetry crystalline structures of mixed-stacking tetralayers. We also note that the exfoliation of tetralayer graphene can produce films where a four-layer system may be adjacent with a thinner or thicker crystal (within the same flake). Therefore, for reference, we also analyzed the different stacking polytypes of tri- and pentalayer graphene systems, for these structures to be distinguished from tetralayer graphene.

All the research data supporting this publication is directly available within this publication.

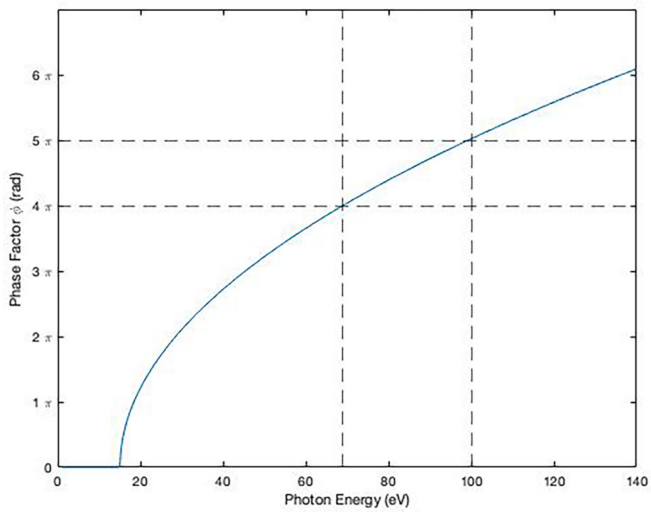

FIG. 8. ARPES spectra phase factor as a function of photon energy ω.

ACKNOWLEDGMENTS

We thank M. Ben-Shalom, D. Beitner, H. Suchowski, and N. Wilson for useful discussions. We acknowledge support from EU Graphene Flagship Project, EPSRC Grants No. EP/S019367/1, No. EP/P026850/1, and No. EP/N010345/1, and EPSRC CDT Graphene-NOWNANO EP/L01548X/1.

APPENDIX A

In this Appendix to complement the trilayer and pentalayer graphene spectra, we offer the reader the band structures and density of states plots of each of these systems. All figures shown below were calculated using analog hybrid $\boldsymbol{k} \cdot \boldsymbol{p}$ theory—tight-binding Hamiltonian's parameterized by the full Slonczewski-Weiss-McClure parameters to those shown in Sec. II above.

APPENDIX B

In this Appendix, we describe how to calculate an estimate of the ARPES spectra phase shift between subsequent layers. As shown above, the out-of-plane momentum of the excited electrons is $p_z = \sqrt{2m(\omega - A) + \epsilon_c - (\hbar K)^2}$, where ϵ_c is the energy the ARPES measurement was taken at. The overall phase shift between subsequent layers is due to the increased path length traveled by electrons emitted from deeper layers and is taken as $\exp(ip_z c_0/\hbar)^{\lambda}$, where c_0 is the interlayer difference of graphene and $\lambda = 0$–3, is the layer number. We know that the dominant term in the out-of-plane momentum is incident photon energy ω, thus, by varying this, we vary the phase shift, see Fig. 8 below.

[1] K. F. Mak, J. Shan, and T. F. Heinz, Electronic Structure of Few-Layer Graphene: Experimental Demonstration of Strong Dependence on Stacking Sequence, Phys. Rev. Lett. **104**, 176404 (2010).

[2] K. G. Wirth, J. B. Hauck, A. Rothstein, H. Kyoseva, D. Siebenkotten, L. Conrads, L. Klebl, A. Fischer, B. Beschoten, C. Stampfer, D. M. Kennes, L. Waldecker, and T. Taubner, Experimental observation of abcb stacked tetralayer graphene, ACS Nano **16**, 16617 (2022).

[3] A. L. Grushina, D.-K. Ki, M. Koshino, A. A. L. Nicolet, C. Faugeras, E. McCann, M. Potemski, and A. F. Morpurgo, Insulating state in tetralayers reveals an even–odd interaction effect in multilayer graphene, Nat. Commun. **6**, 6419 (2015).

[4] C. Yoon, Y. Jang, J. Jung, and H. Min, Broken sublattice symmetry states in bernal stacked multilayer graphene, 2D Mater. **4**, 021025 (2017).

[5] K. Myhro, S. Che, Y. Shi, Y. Lee, K. Thilahar, K. Bleich, D. Smirnov, and C. N. Lau, Large tunable intrinsic gap in rhombohedral-stacked tetralayer graphene at half filling, 2D Mater. **5**, 045013 (2018).

[6] Y. Shi, S. Che, K. Zhou, S. Ge, Z. Pi, T. Espiritu, T. Taniguchi, K. Watanabe, Y. Barlas, R. Lake, and C. N. Lau, Tunable Lifshitz Transitions and Multiband Transport in Tetralayer Graphene, Phys. Rev. Lett. **120**, 096802 (2018).

[7] A. E. Mouhafid and A. Jellal, Band structure and klein paradox for a pn junction in ABCA-tetralayer graphene, arXiv:1903.05676.

[8] S. Che, Y. Shi, J. Yang, H. Tian, R. Chen, T. Taniguchi, K. Watanabe, D. Smirnov, C. N. Lau, E. Shimshoni, G. Murthy, and H. A. Fertig, Helical Edge States and Quantum Phase Transitions in Tetralayer Graphene, Phys. Rev. Lett. **125**, 036803 (2020).

[9] M. Liang, S. Li, and J.-H. Gao, Gate-induced half metals in bernal-stacked graphene multilayers, Phys. Rev. B **105**, 045419 (2022).

[10] Y.-Z. Chou, F. Wu, J. D. Sau, and S. Das Sarma, Acoustic-phonon-mediated superconductivity in moiréless graphene multilayers, Phys. Rev. B **106**, 024507 (2022).

[11] D. Pierucci, T. Brumme, J.-C. Girard, M. Calandra, M. G. Silly, F. Sirotti, A. Barbier, F. Mauri, and A. Ouerghi, Atomic and electronic structure of trilayer graphene/SiC(0001): Evidence of strong dependence on stacking sequence and charge transfer, Sci. Rep. **6**, 33487 (2016).

[12] Y. Shi, S. Xu, Y. Yang, S. Slizovskiy, S. V. Morozov, S.-K. Son, S. Ozdemir, C. Mullan, J. Barrier, J. Yin, A. I. Berdyugin, B. A. Piot, T. Taniguchi, K. Watanabe, V. I. Fal'ko, K. S. Novoselov, A. K. Geim, and A. Mishchenko, Electronic phase separation in multilayer rhombohedral graphite, Nature (London) **584**, 210 (2020).

[13] Z. A. H. Goodwin, L. Klebl, V. Vitale, X. Liang, V. Gogtay, X. van Gorp, D. M. Kennes, A. A. Mostofi, and J. Lischner, Flat bands, electron interactions, and magnetic order in magic-angle mono-trilayer graphene, Phys. Rev. Mater. **5**, 084008 (2021).

[14] P. Tomić, P. Rickhaus, A. Garcia-Ruiz, G. Zheng, E. Portolés, V. Fal'ko, K. Watanabe, T. Taniguchi, K. Ensslin, T. Ihn, and F. K. de Vries, Scattering between Minivalleys in Twisted Double Bilayer Graphene, Phys. Rev. Lett. **128**, 057702 (2022).

[15] J. C. Slonczewski and P. R. Weiss, Band structure of graphite, Phys. Rev. **109**, 272 (1958).

[16] J. W. McClure, Band structure of graphite and de haas-van alphen effect, Phys. Rev. **108**, 612 (1957).

[17] J. W. McClure, Theory of diamagnetism of graphite, Phys. Rev. **119**, 606 (1960).
[18] A. Garcia-Ruiz, H.-Y. Deng, V. V. Enaldiev, and V. I. Fal'ko, Full slonczewski-weiss-mcclure parametrization of few-layer twistronic graphene, Phys. Rev. B **104**, 085402 (2021).
[19] J. Yin, S. Slizovskiy, Y. Cao, S. Hu, Y. Yang, I. Lobanova, B. A. Piot, S.-K. Son, S. Ozdemir, T. Taniguchi, K. Watanabe, K. S. Novoselov, F. Guinea, A. K. Geim, V. Fal'ko, and A. Mishchenko, Dimensional reduction, quantum hall effect and layer parity in graphite films, Nat. Phys. **15**, 437 (2019).
[20] Z. Ge, S. Slizovskiy, F. Joucken, E. A. Quezada, T. Taniguchi, K. Watanabe, V. I. Fal'ko, and J. Velasco, Control of Giant Topological Magnetic Moment and Valley Splitting in Trilayer Graphene, Phys. Rev. Lett. **127**, 136402 (2021).
[21] A. B. Kuzmenko, I. Crassee, D. van der Marel, P. Blake, and K. S. Novoselov, Determination of the gate-tunable band gap and tight-binding parameters in bilayer graphene using infrared spectroscopy, Phys. Rev. B **80**, 165406 (2009).
[22] A. Einstein, Über einen die erzeugung und verwandlung des lichtes betreffenden heuristischen gesichtspunkt, Ann. Phys. **322**, 132 (1905).
[23] C. J. Sayers, H. Hedayat, A. Ceraso, F. Museur, M. Cattelan, L. S. Hart, L. S. Farrar, S. Dal Conte, G. Cerullo, C. Dallera, E. Da Como, and E. Carpene, Coherent phonons and the interplay between charge density wave and mott phases in $1T - TaSe_2$, Phys. Rev. B **102**, 161105(R) (2020).
[24] D.-C. Ryu, C.-J. Kang, J. Kim, K. Kim, G. Kotliar, J.-S. Kang, J. D. Denlinger, and B. I. Min, Topological surface states on the nonpolar (110) and (111) surfaces of SmB_6, Phys. Rev. B **103**, 125101 (2021).
[25] L. Baringthon, T. H. Dang, H. Jaffrès, N. Reyren, J.-M. George, M. Morassi, G. Patriarche, A. Lemaitre, F. Bertran, and P. Le Fèvre, Topological surface states in ultrathin $Bi_{1-x}Sb_x$ layers, Phys. Rev. Mater. **6**, 074204 (2022).
[26] J. J. P. Thompson, D. Pei, H. Peng, H. Wang, N. Channa, H. L. Peng, A. Barinov, N. B. M. Schröter, Y. Chen, and M. Mucha-Kruczyński, Determination of interatomic coupling between two-dimensional crystals using angle-resolved photoemission spectroscopy, Nat. Commun. **11**, 3582 (2020).
[27] M. Mucha-Kruczyński, O. Tsyplyatyev, A. Grishin, E. McCann, V. I. Fal'ko, A. Bostwick, and E. Rotenberg, Characterization of graphene through anisotropy of constant-energy maps in angle-resolved photoemission, Phys. Rev. B **77**, 195403 (2008).
[28] K. F. Mak, M. Y. Sfeir, J. A. Misewich, and T. F. Heinz, The evolution of electronic structure in few-layer graphene revealed by optical spectroscopy, Proc. Natl. Acad. Sci. USA **107**, 14999 (2010).
[29] Y. Wang, G. Yu, M. Rösner, M. I. Katsnelson, H.-Q. Lin, and S. Yuan, Polarization-Dependent Selection Rules and Optical Spectrum Atlas of Twisted Bilayer Graphene Quantum Dots, Phys. Rev. X **12**, 021055 (2022).
[30] K. Yu, N. Van Luan, T. Kim, J. Jeon, J. Kim, P. Moon, Y. H. Lee, and E. J. Choi, Gate tunable optical absorption and band structure of twisted bilayer graphene, Phys. Rev. B **99**, 241405(R) (2019).
[31] C.-J. Kim, A. Sánchez-Castillo, Z. Ziegler, Y. Ogawa, C. Noguez, and J. Park, Chiral atomically thin films, Nat. Nanotechnol. **11**, 520 (2016).
[32] A. B. Kuzmenko, E. van Heumen, F. Carbone, and D. van der Marel, Universal Optical Conductance of Graphite, Phys. Rev. Lett. **100**, 117401 (2008).
[33] B. G. Ghamsari, J. Tosado, M. Yamamoto, M. S. Fuhrer, and S. M. Anlage, Measuring the complex optical conductivity of graphene by fabry-pérot reflectance spectroscopy, Sci. Rep. **6**, 34166 (2016).
[34] K. F. Mak, L. Ju, F. Wang, and T. F. Heinz, Optical spectroscopy of graphene: From the far infrared to the ultraviolet, Solid State Commun. **152**, 1341 (2012).
[35] K. Sasaki and K. Hitachi, Universal layer number in graphite, Commun. Phys. **3**, 90 (2020).
[36] T. Stauber, N. M. R. Peres, and A. K. Geim, Optical conductivity of graphene in the visible region of the spectrum, Phys. Rev. B **78**, 085432 (2008).
[37] T. Stauber, P. San-Jose, and L. Brey, Optical conductivity, drude weight and plasmons in twisted graphene bilayers, New J. Phys. **15**, 113050 (2013).
[38] T. Ando and M. Koshino, Optical absorption by interlayer density excitations in bilayer graphene, J. Phys. Soc. Jpn. **78**, 104716 (2009).
[39] C. J. Tabert and E. J. Nicol, Dynamical conductivity of aa-stacked bilayer graphene, Phys. Rev. B **86**, 075439 (2012).
[40] F. Liang, H. Xu, X. Wu, C. Wang, C. Luo, and J. Zhang, Raman spectroscopy characterization of two-dimensional materials*, Chin. Phys. B **27**, 037802 (2018).
[41] A. C. Ferrari and D. M. Basko, Raman spectroscopy as a versatile tool for studying the properties of graphene, Nat. Nanotechnol. **8**, 235 (2013).
[42] A. Eckmann, A. Felten, A. Mishchenko, L. Britnell, R. Krupke, K. S. Novoselov, and C. Casiraghi, Probing the nature of defects in graphene by raman spectroscopy, Nano Lett. **12**, 3925 (2012).
[43] A. Gupta, G. Chen, P. Joshi, S. Tadigadapa, and Eklund, Raman scattering from high-frequency phonons in supported *n*-graphene layer films, Nano Lett. **6**, 2667 (2006).
[44] T. M. G. Mohiuddin, A. Lombardo, R. R. Nair, A. Bonetti, G. Savini, R. Jalil, N. Bonini, D. M. Basko, C. Galiotis, N. Marzari, K. S. Novoselov, A. K. Geim, and A. C. Ferrari, Uniaxial strain in graphene by raman spectroscopy: *G* peak splitting, grüneisen parameters, and sample orientation, Phys. Rev. B **79**, 205433 (2009).
[45] O. Kashuba and V. I. Fal'ko, Signature of electronic excitations in the raman spectrum of graphene, Phys. Rev. B **80**, 241404(R) (2009).
[46] A. Garcia-Ruiz, S. Slizovskiy, M. Mucha-Kruczyński, and V. I. Fal'ko, Spectroscopic signatures of electronic excitations in raman scattering in thin films of rhombohedral graphite, Nano Lett. **19**, 6152 (2019).
[47] A. García-Ruiz, J. J. P. Thompson, M. Mucha-Kruczyński, and V. I. Fal'ko, Electronic Raman Scattering in Twistronic Few-Layer Graphene, Phys. Rev. Lett. **125**, 197401 (2020).
[48] A. García-Ruiz, M. Mucha-Kruczyński, and V. I. Fal'ko, Superconductivity-induced features in the electronic raman spectrum of monolayer graphene, Phys. Rev. B **97**, 155405 (2018).
[49] A. Garcia-Ruiz, Signatures of electronic excitations in the Raman spectra of graphene materials, Ph.D. thesis, University of Bath, 2020.
[50] P. Moon and M. Koshino, Optical absorption in twisted bilayer graphene, Phys. Rev. B **87**, 205404 (2013).